

Phase Composition and Disorder in $\text{La}_2(\text{Sn,Ti})_2\text{O}_7$ Ceramics: New Insights from NMR Crystallography

Arantxa Fernandes,¹ David McKay,¹ Scott Sneddon,¹ Daniel M. Dawson,¹
Sebastian Lawson,² Richard Veazey,² Karl R. Whittle^{2,3}
and Sharon E. Ashbrook^{1*}

¹*School of Chemistry, EaStCHEM and Centre of Magnetic Resonance, University of St Andrews,
St Andrews KY16 9ST, United Kingdom*

²*Department of Materials Science and Engineering, University of Sheffield,
Mappin Street, Sheffield S1 3JD, UK*

³*School of Engineering, University of Liverpool, Brownlow Hill, Liverpool, L69 3GH, UK*

* Author to whom correspondence should be addressed

Email: sema@st-andrews.ac.uk

Telephone: +44 (0)1334 463779

Submitted to *J. Phys. Chem. C*

Abstract

An NMR crystallographic approach, involving the combination of ^{119}Sn NMR spectroscopy, XRD and DFT calculations, is demonstrated for the characterisation of $\text{La}_2\text{Sn}_{2-x}\text{Ti}_x\text{O}_7$ ceramics. A phase change from pyrochlore ($\text{La}_2\text{Sn}_2\text{O}_7$) to a layered perovskite phase ($\text{La}_2\text{Ti}_2\text{O}_7$) is predicted (by radius ratio rules) to occur when $x \approx 0.95$. However, the sensitivity of NMR spectroscopy to the local environment is able to reveal a significant two-phase region is present, extending from $x = 1.8$ to ~ 0.2 , with limited solid solution at the two extremes, in broad agreement with powder XRD measurements. DFT calculations reveal that there is preferential site substitution of Sn in $\text{La}_2\text{Ti}_2\text{O}_7$, with calculated shifts for Sn substitution onto Ti1 and Ti2 sites (in the “bulk” perovskite layers) in better agreement with experiment than those for Ti3 and Ti4 (“edge” sites). Substitution onto these two sites also produces structural models with lower relative enthalpy. As the Sn content decreases, there is a further preference for substitution onto Sn2. In contrast, the relative intensities of the spectral resonances suggest that Ti substitution into the pyrochlore phase is random, although only a limited solid solution is observed (up to $\sim 7\%$ Ti). DFT calculations predict very similar ^{119}Sn shifts for Sn substitution into the two proposed models of $\text{La}_2\text{Ti}_2\text{O}_7$ (monoclinic ($P2_1$) and orthorhombic ($Pna2_1$)), indicating it is not possible to distinguish between them. However, the relative energy of the Sn-substituted orthorhombic phase was higher than that of substituted monoclinic cells, suggesting that the latter is the more likely structure.

Introduction

The chemical and structural flexibility of the pyrochlore materials ($A_2B_2O_7$) has attracted significant interest in recent years. This has led to a variety of applications, including those related to nuclear fission, with pyrochlores and pyrochlore-based materials being proposed as both matrices for immobilisation and as advanced inert matrix fuels.¹⁻⁵ One of the key criteria for determining the applicability of a material for such applications is how it responds to the damaging effects of radiation, *i.e.*, its propensity to amorphise. An advantage of pyrochlores in this context is their ability to transform to different structures as the composition or conditions vary. The pyrochlore structure (**A**, space group $Fd\bar{3}m$) shown in Figure 1a is an ordered derivative of fluorite (AO_2), with the removal of 1/8 of the oxygen atoms.⁶⁻⁷ This produces two types of cation sites: an eight-coordinate A site (typically occupied by 2+ or 3+ cations), and a six-coordinate B site (usually occupied by smaller 5+ or 4+ cations). The stability of this structure is indicated by the relative ratio of the A and B site cations, r_A/r_B , with pyrochlore stable when this is between 1.46 and 1.78. Below 1.46 a transformation to a defect fluorite structure (with disorder on both cation and anion lattices) is expected while, above 1.78, materials are predicted to adopt a layered perovskite-related ($La_2Ti_2O_7$) structure, as shown in Figure 1b.⁸⁻¹¹ There are four crystallographically-distinct types of La and Ti sites in this structure. Materials that exhibit this structural type have been investigated for uses in photocatalysis and electrical applications that exploit their piezoelectric and ferroelectric properties.¹²⁻¹³ There has been some debate over the exact structure adopted by $La_2Ti_2O_7$ itself, with two suggested forms; monoclinic ($P2_1$)⁸ (**B**, Figure 1b) and orthorhombic ($Pna2_1$)⁹ (**C**, see Supporting Information Figure S1.1). The structures have two similar unit cell lengths (of ~ 7.8 and ~ 5.5 Å), with the remaining length twice as large in **C** than in **B** (see the Supporting Information for more detail). Although subsequent work appears to confirm the presence of a monoclinic structure, it is not clear whether an orthorhombic modification exists, or whether the twinned nature of the crystals studied led to an incorrect choice of symmetry in the earlier work.⁸⁻¹¹

The physical and chemical properties of ceramics are intimately linked to their local structure and disorder. However, the study of disordered materials can be challenging, particularly if more than one phase is present, with many diffraction-based approaches providing information only on the average structure. Nuclear magnetic resonance (NMR) spectroscopy, with its sensitivity to the local structural environment, without the need for any long-range order, has proven a useful element-specific and complementary tool when studying disorder in solids, with both the isotropic chemical shift and the chemical shift anisotropy (CSA) shown to be highly dependent on the number, nature and position of the surrounding atoms.¹⁴⁻¹⁵ More recently, the simultaneous use of theoretical calculations alongside experiment has seen a significant increase in popularity, aiding the interpretation and assignment of the complex spectra that are frequently observed for disordered solids.¹⁶⁻¹⁷ This combined approach (often termed NMR crystallography) has previously been applied to the investigation of cation disorder in $Y_2(\text{Sn,Ti})_2\text{O}_7$ pyrochlore solid solutions, demonstrating no significant mixing of the A and B sites cations were observed, but that Sn and Ti were randomly distributed on the B sites.¹⁸⁻²⁰ More recently, NMR crystallography was applied to the $Y_2(\text{Sn,Zr})_2\text{O}_7$ compositional series, where a transition to a defect fluorite phase was expected for Zr-rich compositions.²¹ NMR was able to demonstrate the presence of a significant two-phase region in this series, from $Y_2\text{Sn}_{1.8}\text{Zr}_{0.2}\text{O}_7$ to $Y_2\text{Sn}_{0.4}\text{Zr}_{1.6}\text{O}_7$, with the compositions of the phases present shown to differ greatly.

In this work, we utilise NMR spectroscopy and density functional theory (DFT) calculations to study $\text{La}_2(\text{Sn,Ti})_2\text{O}_7$, where a phase transition from a pyrochlore ($\text{La}_2\text{Sn}_2\text{O}_7$, where $r_A/r_B = 1.68$) to a layered perovskite phase ($\text{La}_2\text{Ti}_2\text{O}_7$, where $r_A/r_B = 1.92$) is expected. We exploit a combination of experiment and computation to consider the number and composition of the phases present for each of the nominal starting compositions, and how the phase transition progresses. We also use DFT calculations to investigate the preferred position and distribution of the substituted cations in each of the

two phases, and consider the consistency of our data with the suggested (*i.e.*, **B** and **C**) structural models for $\text{La}_2\text{Ti}_2\text{O}_7$. This NMR crystallographic study provides more detailed structural information than is available from laboratory X-ray diffraction, and demonstrates the future potential of this approach for the investigation of disordered solids.

Experimental and Computational Methods

Synthesis: Samples in the system $\text{La}_2\text{Sn}_{2-x}\text{Ti}_x\text{O}_7$ were prepared in two batches, the first batch consisting of 11 samples from $x = 0$ to $x = 2$, in steps of 0.2. Subsequently, a second batch of samples from $x = 1.8$ to $x = 1.95$ (with x varying in steps of 0.05) was prepared. Both sets of samples were prepared under identical conditions, using stoichiometric amounts of La_2O_3 (Sigma-Aldrich 99.9 %), TiO_2 (Sigma-Aldrich 99 %) and SnO_2 (Sigma-Aldrich 99.9 %), which were pre-dried overnight to remove CO_2 and H_2O before weighing. These powders were then ball milled for 16 hours in isopropanol with zirconia media, dried, sieved and (uniaxially) pressed into pellets. The pellets were then heated at 1673 K for 48 hours, with a ramp rate of 5 K min^{-1} . After cooling, the samples were ground for both X-ray diffraction and MAS NMR analysis.

X-ray diffraction: Structural analysis was undertaken by X-ray powder diffraction using a Bruker D2 Phaser, with weighted Cu K_α ($\lambda = 1.54184 \text{ \AA}$) radiation. The angular range was 5° to 90° with a step size of 0.02° and a step duration of 0.4 s. Powder patterns are shown in the Supporting Information, across two compositional ranges, with Figure S2.1 showing the complete compositional range and Figure S2.2 from $\text{La}_2\text{Ti}_2\text{O}_7 - \text{La}_2\text{Ti}_{1.6}\text{Sn}_{0.4}\text{O}_7$.

NMR spectroscopy: NMR spectra were acquired using a Bruker Avance III spectrometer, equipped with a 9.4 T widebore magnet operating at a Larmor frequency of 149.2 MHz for ^{119}Sn . Powdered samples were packed into a 4.0 mm ZrO_2 rotor and rotated at a rate of 14 kHz, using a conventional 4 mm HX probe. Spectra were acquired using a radiofrequency

field strength of ~ 111 kHz ($\pi/2 \approx 2.25$ μ s) and a recycle interval of 30 s, and are the result of averaging between 16 and 10688 transients. Spectra were acquired using either a spin echo (to ensure accurate acquisition of any broader components) or a Carr-Purcell-Meiboom-Gill (CPMG)²²⁻²³ echo train to increase sensitivity. In the latter case, 50 echoes were typically acquired, with a frequency-domain spikelet spacing of between 70 and 100 Hz. Chemical shifts are shown (in ppm) relative to $(\text{CH}_3)_4\text{Sn}$, measured using a secondary reference of SnO_2 ($\delta = -604.3$ ppm).²⁴ The integrated intensities of the spectral resonances were determined using dmfit.²⁵ CSA parameters were measured using slow MAS ($\text{La}_2\text{Sn}_2\text{O}_7$, 2 kHz MAS) or CSA-amplified PASS experiments ($\text{La}_2\text{Sn}_{2-x}\text{Ti}_x\text{O}_7$ with $x = 0.2, 0.4$ and 0.6), using the pulse sequence of Orr *et al.*²⁶⁻²⁷ PASS-based experiments were carried out at an MAS rate of 10 kHz, and a total scaling factor, N_{Tr} , of 6.67, resulting in an apparent MAS rate of 1.5 kHz in the indirect dimension. Spectra are the result of averaging between 78 and 182 transients for each of 16 rows, with a recycle interval of 30 s. Fitting of the sideband patterns in the indirect dimension was carried out using SIMPSON,²⁸ by comparison to a one-dimensional MAS spectrum (assuming ideal pulses). The root-mean-square (rms) error quoted is that output by SIMPSON, as described in the SIMPSON manual.²⁸ See the Supporting Information for further information.

Calculations: Periodic DFT calculations were carried out using the CASTEP code (version 8.0) and adopted the PBE exchange-correlation functional.²⁹⁻³¹ Core-valence interactions were described by ultrasoft pseudopotentials,³² taking ZORA scalar relativistic effects into account.³³ A planewave energy cutoff of 50 Ry was used. The first Brillouin zone was sampled through a Monkhorst-Pack grid with a k-point spacing of 0.05 $2\pi/\text{\AA}$. Optimisation of atomic coordinates and unit/supercell parameters was carried out starting from literature crystal structures⁸⁻⁹ or following Sn/Ti substitutions where appropriate. NMR parameters were computed on the optimised structures employing the gauge-including projector augmented wave (GIPAW) approach³⁰ to reconstruct the all-electron wavefunction in the presence of a magnetic field. Calculations were performed either on a cluster at the University of St Andrews, consisting of 300 12-core Intel

Westmere nodes, connected with QDR Infiniband or, for larger systems, on ARCHER, the UK High Performance Computing service, a Cray XC30 MPP supercomputer with 4920 24-core Intel Ivy Bridge nodes. Diagonalisation of the absolute shielding tensor (σ), yields the three principal components, σ_{11} , σ_{22} and σ_{33} , from which the principal components of the shift tensor, δ_{ii} , can be generated using $\delta_{ii} = -(\sigma_{ii} - \sigma_{\text{ref}}) / (1 - \sigma_{\text{ref}}) \approx -(\sigma_{ii} - \sigma_{\text{ref}})$, ordered such that $\delta_{11} \geq \delta_{22} \geq \delta_{33}$. The reference shielding, σ_{ref} (assumed to be $\ll 1$), was determined (by comparing the calculated absolute shielding in $\text{La}_2\text{Sn}_2\text{O}_7$ to experiment) to be 3243.25 ppm for ^{119}Sn . The isotropic shift, δ_{iso} , is then given by $\delta_{\text{iso}} = (\delta_{11} + \delta_{22} + \delta_{33})/3$. The anisotropy is defined by the span, $\Omega = \delta_{11} - \delta_{33}$, and the skew, $\kappa = 3(\delta_{22} - \delta_{\text{iso}})/\Omega$ is a measure of the asymmetry of the tensor. Computed structures and NMR parameters were processed using Python scripts extending the CCP-NC MagresPython module.³⁴

Results and discussion

Cation substitution in $\text{La}_2\text{Sn}_{2-x}\text{Ti}_x\text{O}_7$ is expected to lead to a change from pyrochlore (for Sn-rich compositions) to a layered perovskite structure as the Ti content increases. This change is predicted, by simple radius ratio considerations,⁷ to occur at $x \approx 0.95$. Figure 2 shows ^{119}Sn MAS NMR spectra of $\text{La}_2(\text{Sn},\text{Ti})_2\text{O}_7$, acquired using a spin echo pulse sequence. The spectrum of the end member, $\text{La}_2\text{Sn}_2\text{O}_7$ contains a single sharp resonance, at -642 ppm, in good agreement with the previous literature.³⁵ This corresponds to six-coordinate Sn, confirming that Sn exclusively occupies the B site in the ordered pyrochlore structure. A spectrum of $\text{La}_2\text{Sn}_2\text{O}_7$ acquired using slow MAS (see the Supporting Information) reveals that the ^{119}Sn Ω is 43 (5) ppm and κ is -0.93 (5). This is in reasonable agreement with values calculated using DFT ($\Omega = 58$ ppm and $\kappa = -1.0$).

When $x = 0.2$, two additional sharp resonances are observed, at -647 and -653 ppm, most likely arising from substitution of Ti into the next-nearest neighbor (NNN) B sites in the pyrochlore structure, **A**. The assignment of the resonances can be confirmed using DFT calculations (following the approach outlined in Ref. 18 (described in more detail in the

Supporting Information), where the local environment of one of the Sn atoms in the unit cell of $\text{La}_2\text{Sn}_2\text{O}_7$ is systematically modified to include increasing numbers of Ti cations on the six surrounding B sites). Figure 3a shows the calculated ^{119}Sn δ_{iso} as the number of Sn and Ti NNN are varied. The calculations confirm a decrease in the average ^{119}Sn δ_{iso} (of ~5 ppm) as the first Ti is substituted into the NNN sites, although a range of shifts (of 10 ppm) is observed for each type of NNN environment, as a result of variation in the longer-range structure. A smaller decrease in the average ^{119}Sn δ_{iso} is observed upon the substitution of a second Ti, while further substitution appears to result in small shifts back to higher δ (although it should be noted that relatively few points are available for environments with very high Ti content, owing to the nature of the model used, *i.e.*, substitution into a unit cell of $\text{La}_2\text{Sn}_2\text{O}_7$). While perhaps a little unexpected, this behaviour is reminiscent of that observed for ^{119}Sn NMR of $\text{Y}_2(\text{Sn},\text{Ti})_2\text{O}_7$ and $\text{Y}_2(\text{Sn},\text{Zr})_2\text{O}_7$ pyrochlores in earlier work.^{18,21} A similar plot, against calculated Ω is shown in Figure 3b, and reveals a similar trend, with an increase in Ω (of 10-15 ppm) when one Ti is substituted onto the NNN B sites, but a decrease in Ω when a much greater number of Ti are substituted.

Owing to the difficulties associated with measuring Howev parameters using slow MAS experiments, particularly if the CSA is small and if there is more than one site present, CSA-amplified PASS experiments²⁶⁻²⁷ were employed (see the Supporting Information for more detail). For $\text{La}_2\text{Sn}_{1.8}\text{Ti}_{0.2}\text{O}_7$, $\text{La}_2\text{Sn}_{1.6}\text{Ti}_{0.4}\text{O}_7$ and $\text{La}_2\text{Sn}_{1.4}\text{Ti}_{0.6}\text{O}_7$, Sn species having Sn6 NNN environments had Ω of ~46 ppm. An increase in Ω was observed for resonances assigned as having Sn5Ti NNN, as predicted by the DFT calculations. For all three materials, the peak corresponding to this environment appeared to consist of two overlapping contributions in the amplified PASS experiments (as shown in the Supporting Information) probably arising from small differences in the longer-range structure. Sideband manifolds extracted for both had similar Ω values, of 54-60 ppm. Owing to its low intensity, it was not possible to extract Ω for the resonance at -653 ppm. Although, in general, the calculated Ω appears slightly overestimated when compared to experiment, the computed and experimental trends are in good agreement, and so support the spectral

assignment. Previous ^{89}Y CSA measurements on related pyrochlore materials²⁰ applied a scaling factor to calculated values of Ω for comparison to experiment. This approach has not been employed here owing to the relatively small amount (and the small range) of data available, and only the trends and variations in the measurements are considered.

The calculations represented by Figure 3 confirm that the resonances at -647 and -653 ppm can be assigned to Sn species with Sn5Ti and Sn4Ti2 NNN environments, respectively. However, it is also suggested that it may be difficult to separate and assign resonances corresponding to Sn with differing NNN environments in the pyrochlore phase as the Ti content increases, hence complicating any analysis. However, it should be noted that the relative intensity of the sharp pyrochlore resonances observed varies very little as x increases, perhaps suggesting that there is limited substitution of Ti into this phase. The three sharp signals persist throughout the compositional range shown in Figure 2, through to $x = 1.8$ (which, from radius ratio considerations, should exhibit a layered perovskite structure). This raises the question of whether ^{119}Sn signals from the layered perovskite-like phase simply appear at similar shifts to those from the pyrochlore, or whether a pyrochlore phase is indeed present from $x = 0.2$ to $x = 1.8$.

As it is not possible to predict NMR parameters for the Sn-free end member $\text{La}_2\text{Ti}_2\text{O}_7$, to provide further insight DFT calculations were performed for a monoclinic unit cell of $\text{La}_2\text{Sn}_{0.125}\text{Ti}_{1.875}\text{O}_7$ by substitution of one Ti atom with one Sn atom in **B**. As four crystallographically-distinct Ti sites are present (Ti1, Ti2, Ti3 and Ti4), four separate structural models, with Sn placed on each of these sites, were constructed before performing geometry optimisation and NMR calculations (see Experimental and Computational Methods). The predicted ^{119}Sn δ_{iso} values are shown in Figure 4 and are given in Table 1. The values range between -584 and -619 ppm, suggesting that the signal at ~ -650 ppm does not result from the layered perovskite phase. The signal in this region can, therefore, be assumed to result from a pyrochlore phase, suggesting a significant two-phase region is present within the series. Figure 4 and Table 1 also show that Sn/Ti

substitutions in **C**, (*i.e.*, $\text{La}_2\text{Sn}_{0.125}\text{Ti}_{1.875}\text{O}_7$, with sites numbered for consistency with the monoclinic form, see the Supporting Information Figure S1.1), give a similar conclusion, with predicted shifts between -583 and -616 ppm. In light of these computational results, a second set of $\text{La}_2(\text{Sn,Ti})_2\text{O}_7$ samples was prepared with x varying from 1.80 to 1.95 in steps of 0.05. Owing to the low level of Sn in these materials, ^{119}Sn spectra were acquired using CPMG experiments, and are shown (as spikelets) in Figure 5. CPMG spectra provide greater peak-height signal, but can be less quantitative if there are any significant T_2 differences between the signals. Above $x = 1.85$, no signal from the pyrochlore phase is observed between -640 and -655 ppm, indicating that this represents the upper limit of the two-phase region observed.

Interestingly, Figure 4 shows that the predicted ^{119}Sn shifts for the layered perovskite phase agree with the resonance positions measured experimentally only when Sn is placed on the perovskite-like Ti1 and Ti2 sites, suggesting there may be a preference for Sn substitution into these sites (alternative sites, Ti3 and Ti4, are denoted as “edge sites”, as shown in Figure 1b). The calculated ^{119}Sn shifts are in reasonable agreement with experiment for single Sn substitutions in both **B** and **C** forms, and so cannot prove conclusively which structural model is most accurate. In both cases, two of the unit cell dimensions are relatively short, corresponding to a repeat unit of just two TiO_6 octahedra. For **B**, substitution of one Sn corresponds to a doping level of 12.5% (*i.e.*, 1/8 of the Ti sites in the unit cell), higher than that in many of the spectra shown in Figure 2. The periodic nature of the calculations also results in an artificially ordered structure with O-bridged, alternating Sn and Ti cations along the crystallographic a direction. In order to consider the effects of such ordering upon the calculated ^{119}Sn δ_{iso} values (by better isolating substituted Sn cations) an additional set of DFT calculations were also performed on a $2 \times 1 \times 1$ supercell of **B**, termed **B^{SC}**. Sn/Ti substitutions were made into each of the four distinct Ti sites, giving $\text{La}_2\text{Sn}_{0.125}\text{Ti}_{1.875}\text{O}_7$ (see the Supporting Information for more detail). As shown in Figure 4 and Table 1, the calculated ^{119}Sn shifts are very similar between **B^{SC}** and **B**, and match experiment only for Sn1/Ti1 and Sn2/Ti2 substitutions, again

suggesting preferential substitution into these sites. This conclusion is also supported by the relative enthalpies, ΔH , of the substituted models, as shown in Figure 4, for each of the three series of calculations. The range of relative enthalpies is relatively small, however, the most stable structures correspond to the same substitutions that produce ^{119}Sn shifts in agreement with experiment. Enthalpy differences between the four structures calculated from **B** are given relative to the most thermodynamically stable structure, *i.e.*, that with Sn2/Ti2. This is followed by substitution into Ti1 ($\Delta H = 0.01$ eV), Ti3 ($\Delta H = 0.05$ eV) and finally Ti4 ($\Delta H = 0.11$ eV). For the **B^{SC}** and **C** models, since these have equivalent composition, ΔH can be renormalized to Sn2/Ti2 substitution in **B^{SC}**, placing both series on the same relative enthalpy scale. While the differences in ΔH are again small, the same trend is seen as in the **B** series. For **B^{SC}** and **C**, Sn2/Ti2 substitution is most favourable ($\Delta H = 0.00$ and 0.04 eV, respectively), then Sn1/Ti1 substitution ($\Delta H = 0.02$ and 0.05 eV respectively), Sn3/Ti3 ($\Delta H = 0.07$ and 0.07 eV, respectively) and Sn4/Ti4 ($\Delta H = 0.13$ and 0.14 eV for **B^{SC}** and **C** respectively). Of further note is that equivalent substitutions in the **C** series are typically of higher enthalpy than in the **B^{SC}** series, although Sn substitution appears to amplify this difference, as undoped **B^{SC}** is only 0.01 eV more stable than undoped **C**.

The use of supercell calculations based on the monoclinic **B^{SC}** structure (and unit cell models based on **C**), with a single Sn substitution, enabled a doping level of 6.25% to be considered computationally and resulted in Sn atoms that are relatively isolated in the structure (*i.e.*, Sn \cdots Sn distances > 7 Å). However, given the suggestion of preferential site substitution raised by the predicted ^{119}Sn shifts, the possibility of a non-random spatial distribution of Sn (*i.e.*, Sn clustering) should also be considered. Furthermore, a variation in the Sn local environment (*e.g.*, in NNN atoms) might also result in a significant change in δ_{iso} for Sn on Ti3 and Ti4 sites, perhaps bringing these into better agreement with the experimentally-measured shifts. To investigate this, a further series of supercell models, each based on **B^{SC}** with two Sn atom substitutions, was constructed. In separate supercells, a first Sn/Ti substitution was made for each of Ti1, Ti2, Ti3 and Ti4 sites and a second Sn

was substituted into selected Ti sites within a radius of *ca.* 6 Å of the first. To limit computational expense, the second Sn atoms within a supercell were placed to account for one from each group of Ti sites at similar distances (and, therefore, assumed to give a similar effect). For example, in the case of Sn1/Ti1 and Sn2/Ti2 substitutions, within the adopted supercell, pairs of these sites lie at distances of 3.860 and 3.940 Å and at 5.694 and 5.700 Å; here, only combinations at 3.940 and 5.700 Å were considered. A total of 16 di-substituted models were thus generated and were subjected to geometry optimisation and NMR calculations (see the Supporting Information Table S4.1 for detailed results). Calculated ^{119}Sn isotropic chemical shifts are shown in Figure 6 and given in Table S4.1.

Figure 6 shows that the variation in local environment introduced in the di-substituted structures results in a wider range of predicted shifts for each Sn site compared to those predicted for mono-substituted \mathbf{B}^{SC} structures. When the Sn NNN environment is varied, the majority of shifts for di-substituted models including Sn/Ti1 and Sn2/Ti2 substitutions remain in good agreement with the signal seen experimentally and with those for the mono-substituted models. For models with Sn3/Ti3 and Sn4/Ti4 all calculated shifts lie outside the signal seen experimentally. Two cases of Sn1/Ti1 and Sn2/Ti2 substitutions appear to result in ^{119}Sn shifts outside the experimental range (denoted by arrows in Figure 6). Although this may be due to a systematic overestimation of the shifts in the calculations (*i.e.*, all are shifted upfield with respect to experiment), this error is minimised by referencing. Alternatively, the arrangement of Sn atoms leading to these shifts may not arise in the experimental system; for the Sn1 shift at -610 ppm, the second Sn is on the Ti3 site, while for the Sn2 shift at -611 ppm, the second Sn is on the Ti4 site. Therefore, since Sn appears to substitute preferentially into the Ti1 and Ti2 sites these combinations may not occur at any significant level. Finally, it is noted that the level of noise in the experimental spectrum is such that the presence of a low intensity signal around -610 ppm cannot be completely ruled out. No correlations were found between predicted ^{119}Sn shifts or relative enthalpies and Sn...Sn internuclear distance and, therefore, no evidence for Sn clustering was found. However, with the trends between δ_{iso}

and ΔH and Sn/Ti substitution site noted above, it appears the particular site(s) of Sn/Ti substitution, rather than the distance between a given pair of Sn atoms, is the more significant factor affecting these quantities.

Figure 6 suggests that the signal seen at the highest ^{119}Sn chemical shifts experimentally results from Sn2/Ti2 substitution, and that at slightly lower shift to Sn1/Ti1. However, Figure 5 reveals that as x increases the relative intensity of the signals in these two regions varies, suggesting that, when present at very low concentrations, Sn preferentially substitutes onto the Ti2 site, with the amount of Sn1/Ti1 substitution increasing as the Sn content rises. Although the differences in the calculated enthalpies are small, it should be noted that Sn2/Ti2 substitution (considering the substitution of one atom per cell) does also have the lowest relative enthalpy for **B** and **B^{SC}** models.

Although it is clear from Figure 5 that a two-phase region extends in this series to $x = 1.8$, it is not clear from the MAS spectra in Figure 2 exactly where the lower boundary of this region lies. To clarify this, ^{119}Sn CPMG spectra of samples with $x = 0.2$ and 0.4 were acquired, and are shown as insets in Figure 2. Although a low intensity signal is observed for $x = 0.4$ at ~ -580 ppm, no signal is seen for $x = 0.2$ (after ~ 24 hours of acquisition), suggesting that the two-phase region is present from $x = 0.4$ to 1.8 .

Figure 7a plots the %Sn in the pyrochlore and layered perovskite phases against the composition of the initial synthesis mixture. A small increase in the amount of Sn in the layered perovskite phase is observed between $x = 0.4$ and 1.2 , before a more significant increase is seen from $x = 1.4$. Above $x = 1.80$ Sn is only found in the layered perovskite phase. Note that the intensity of the peaks attributed to this phase is very low when $x < 1$, resulting in a significant uncertainty in the measurement. The relative intensity of the two sets of peaks is not able to provide information directly on the proportion of the two phases present, since Sn may not be distributed equally between them. However, the composition of the two phases, and, therefore, their proportions, can be obtained from the

relative intensities of the peaks attributed to the pyrochlore phase. If it is assumed that the peaks at -641 , -647 and -653 ppm, arise from Sn species with Sn₆, Sn₅Ti and Sn₄Ti₂ NNN environments, their relative intensities can then provide information on the proportions of Sn and Ti present in this phase for each sample. From this, the starting composition and the relative intensities of the total peaks attributed to the pyrochlore and layered perovskite phases, it is then possible to determine both the composition of the layered perovskite phase and the relative proportions of the two phases present for any starting composition. An example calculation is given in the Supporting Information. The proportion (expressed as %) of the two phases present, and their relative compositions, are plotted in Figures 7b and 7c, respectively. Although no significant signal attributed to the layered perovskite phase can be seen when $x = 0.2$, this analysis suggests a very small amount of this phase is present ($\sim 3.5\%$) but that it contains almost no Sn. The proportion of the layered perovskite phase increases almost linearly as x increases, until it is the major phase (after $x = 1.0$), and the only phase after $x = 1.8$. There appears to be a relatively low solid solution limit for Ti into the stannate pyrochlore, with a maximum of $\sim 7-8\%$ (*i.e.*, La₂Sn_{0.15}Ti_{1.85}O₇), with the variation observed probably resulting from the errors in obtaining accurate relative intensities for compositions where the Sn signal for any one phase is low. There is more variation in the composition of the layered perovskite phase, varying from 100% Ti to 75% Ti as x decreases, although the margin of error becomes significant when $x < 1.0$ owing to the low intensity of the resonance.

In order to undertake the analysis described and produce the results shown in Figure 7, it must be assumed that the pyrochlore peaks observed can be attributed solely to NNN environments of Sn₆, Sn₅Ti and Sn₄Ti₂. Figure 3 predicted some overlap of signals from differing NNN environments at higher x although, as shown in Figure 7, the relatively low level of Ti that appears to be substituted into this phase supports the validity of the assumption above. The approach used, however, also requires a very accurate analysis of the relative intensities of all three pyrochlore peaks. An alternative approach is possible, requiring only an accurate determination of the intensity of the peak

ascribed to an environment with Sn6 NNN (relative to all other signals), but does then assume that there is a random distribution of the B site cations in the pyrochlore phase. If this is true, simple statistics shows that the probability of finding Sn with 6 Sn NNN is directly related to the proportion of Sn in the material (and therefore the composition), with $p(6 \text{ Sn NNN}) = (x/2)^6$ (see the Supporting Information for a more detailed explanation). The relative proportions of each phase present (and their compositions) determined using this alternative approach are almost identical to those determined previously, as shown in the Supporting Information, both (i) confirming the validity of the first method (despite the more stringent requirement for accurate relative intensities for all peaks) and (ii) suggesting that the low number of Ti cations in the pyrochlore phase are, indeed, distributed randomly.

Conclusions

^{119}Sn NMR spectroscopy has been used to investigate $\text{La}_2(\text{Sn,Ti})_2\text{O}_7$, providing detailed insight into the number and proportion of phases present, and the local atomic-level environments observed. A broad two-phase region is present in the series, with limited solid solution at each end of the compositional range. The conclusions are in broad agreement with powder XRD measurements (shown in the Supporting Information). Although the quality of these laboratory data is not sufficient to carry out multiple-phase refinements and determine the proportions and compositions of the phases present, it is clear that the [222] reflection of the pyrochlore phase is first seen when $x = 1.8$. Similarly, Figure S2.1 shows evidence of the [211] reflection of a $\text{La}_2\text{Ti}_2\text{O}_7$ based phase when $x = 0.4$, but not at $x = 0.2$. This is in agreement with the ^{119}Sn NMR spectra in Figure 2, although detailed analysis of the spectral intensities of the pyrochlore phase suggest the possibility of a very small amount (<3%) of layered perovskite phase present when $x = 0.2$, but that this contains no Sn.

At the Sn-rich end of the series, there appears to be a solid-solution limit of 7-8% of Ti into the pyrochlore phase, and the relative intensities of the spectral resonances seen confirm that the cation substitution is random. This is not the case for Ti-rich layered-perovskite phase, where DFT calculations suggest preferential substitution of Sn into just two of the four distinct Ti sites. These correspond to the sites in the bulk of the perovskite layer, rather than those on the edge. As the Sn content decreases further, substitution into Ti2 appears to be preferred, with this arrangement giving the lowest energy (from DFT) and producing calculated ^{119}Sn δ_{iso} that are in best agreement with those seen experimentally. Preferential substitution of Y into $\text{La}_2\text{Ti}_2\text{O}_7$ was also observed in earlier work using ^{89}Y NMR spectroscopy.³⁶ Four distinct resonances could be identified within the NMR spectrum, attributed to Y substitution onto the four distinct A sites present. The relative intensity of these varied with Y content, suggesting preferential substitution of Y onto two of the four sites at La-rich compositions.³⁶ There appears to be a maximum of ~25-30% Sn substitution into the layered perovskite phase in the current work, although the errors inherent in the accurate integration of the spectral resonances as the Sn content increases are larger.

The DFT calculations predict very similar ^{119}Sn shifts for Sn substitution into the two proposed models of $\text{La}_2\text{Ti}_2\text{O}_7$, indicating it is not possible to distinguish between them by NMR spectroscopy. However, it should be noted that the relative energy of the Sn-substituted orthorhombic phase was higher than that of substituted monoclinic cells, suggesting that the latter is a more accurate structural model, in agreement with the conclusions of a number of diffraction-based investigations.¹⁰⁻¹³

Although we have focused on ^{119}Sn NMR in this work, as it has spin quantum number $I = 1/2$, and high-resolution spectra can be easily obtained, it may well be possible to obtain further information from the other (quadrupolar) nuclei present in the materials. While wideline NMR spectra for ^{139}La and $^{47/49}\text{Ti}$ could be obtained, the challenges in measuring small changes in very broad lineshapes (and the additional line broadening

resulting from the distribution of local environments), makes the extraction of detailed information difficult. However, ^{17}O NMR spectroscopy offers an easier, and potentially more informative, approach for studying cation disorder, with O directly coordinated to the cations studied. We are currently investigating the conditions required for quantitative ^{17}O enrichment of a range of pyrochlores and related ceramics (including $\text{La}_2\text{Ti}_2\text{O}_7$ and $\text{La}_2\text{Sn}_2\text{O}_7$), and the parameters required to ensure quantitative spectra can be obtained. Once successful, we will consider whether ^{17}O NMR spectroscopy can provide more detailed information on the cation disorder and preferential substitution in this system.

In summary, this work highlights the detailed information that is available from accurate analysis of quantitative NMR spectra, and confirms the advantages of an NMR crystallography approach for structural characterisation – with the combination of NMR, XRD and DFT calculations able to provide a detailed picture of phase distribution, composition and cation ordering in ceramic oxides.

Acknowledgements

SEA would like to thank the ERC (EU FP7 Consolidator Grant 614290 “EXONMR”) and EPSRC for computational support through the Collaborative Computational Project on NMR Crystallography (CCP-NC), *via* EP/M022501/1, and for other support EP/M506631/1 (SS). SEA would also like to thank the Royal Society and Wolfson Foundation for a merit award. Some of the calculations were performed on the ARCHER UK National Supercomputing Service, and were supported by CCP-NC. KRW acknowledges funding by the EPSRC, (EP/L005581/1), and NGN CDT (EP/L015390/1) and Nuclear First DTC (EP/G037140/1) for PhD funding (RV and SML). The research data (and/or materials) supporting this publication can be accessed at <http://dx.doi.org/10.17630/e30fff33-ddb4-4b87-8d86-245bd3529ad8>.

Supporting Information Available: Further information on the proposed structural models of $\text{La}_2\text{Ti}_2\text{O}_7$, powder XRD analysis, slow MAS and CSA-amplified PASS spectra, DFT calculations and spectral analysis can be found in the Supporting Information. This material is available free of charge via the Internet at <http://pubs.acs.org>.

References

1. Kumar, M.; Raj, I. A.; Pattabiraman, R. $\text{Y}_2\text{Zr}_2\text{O}_7$ (YZ)-Pyrochlore Based Oxide as an Electrolyte Material for Intermediate Temperature Solid Oxide Fuel Cells (ITSOFCs)—Influence of Mn Addition on YZ. *Mater. Chem. Phys.* **2008**, *108*, 102-108.
2. Orera, A.; Slater, P. R. New Chemical Systems for Solid Oxide Fuel Cells. *Chem. Mater.* **2010**, *22*, 675-690.
3. Lumpkin, G. R. Ceramic Waste Forms for Actinides. *Elements*, **2006**, *2*, 365-372.
4. Zhang, Y.; Stewart, M. W. A.; Carter, M. L.; Vance E. R.; Moricca, S. Zirconolite-Rich Titanate Ceramics for Immobilisation of Actinides - Waste form/HIP Can Interactions and Chemical Durability. *J. Nucl. Mater.* **2009**, *395*, 69-74.
5. Ewing, R.; Weber W. J.; Lian, J. Nuclear waste disposal-pyrochlore ($\text{A}_2\text{B}_2\text{O}_7$): Nuclear Waste Form for the Immobilization of Plutonium and “Minor” Actinides. *J. Appl. Phys.* **2004**, *95*, 5949-5971.
6. Subramanian, M. A.; Aravamudan M. A. G.; Subba Rao, G. V. Oxide Pyrochlores – a Review. *Solid State Chem.* **1983**, *15*, 55-143.
7. Chakoumakos, B. C. Systematics of the Pyrochlore Structure Type, Ideal $\text{A}_2\text{B}_2\text{X}_6\text{Y}$. *J. Solid State Chem.* **1984**, *53*, 120-129.
8. Gasperin, P. R. Ditungstate de Lanthane. *Acta Cryst.* **1975**, *B31*, 2129-2130.
9. Scheunemann, K.; Mueller-Buschbaum, H. B. Zur Kristallstruktur von $\text{La}_2\text{Ti}_2\text{O}_7$. *J. Inorg. Nucl. Chem.*, **1975**, *37*, 1879-1881.
10. Schmalle, H. W.; Williams, T.; Reller, A. The Twin Structure of $\text{La}_2\text{Ti}_2\text{O}_7$: X-ray and Transmission Electron Microscopy Studies. *Acta Cryst.* **1993**, *B49*, 235-244.
11. Tanaka, M.; Sekii, H.; Ohi, K. Structural Study of $\text{La}_2\text{Ti}_2\text{O}_7$ by Convergent-Beam Electron Diffraction and Electron Microscopy. *Jpn. J. Appl. Phys.* **1985**, *24*, 814-816.
12. Kim, H. G.; Hwang, D. W.; Bae, S. W.; Jung, J. H.; Lee, J. S. Photocatalytic Water Splitting over $\text{La}_2\text{Ti}_2\text{O}_7$ Synthesized by the Polymerizable Complex Method. *Catal. Lett.*, **2003**, *91*, 193-198.

13. Nanamatsu, S.; Kimura, M.; Doi, K.; Matsushita, S.; Yamada, N. A New Ferroelectric: $\text{La}_2\text{Ti}_2\text{O}_7$. *Ferroelectrics*, **1974**, *8*, 511-513.
14. Ashbrook, S. E.; Dawson, D. M.; Griffin, J. M. in: *Local Structure Characterisation*, John Wiley & Sons Ltd, 1st edn. 2014.
15. Apperley, D. C.; Harris, R. K.; Hodgkinson, P. *Solid State NMR Basic Principles and Practice*, Momentum Press, New York, 2012.
16. Bonhomme, C.; Gervais, C.; Babonneau, F.; Coelho, C.; Pourpoint, F.; Azaïs, T.; Ashbrook, S. E.; Griffin, J. M.; Yates, J. R.; Mauri, F.; Pickard, C. J. First-Principles Calculation of NMR Parameters Using the Gauge Including Projector Augmented Wave Method: A Chemist's Point of View. *Chem. Rev.* **2012**, *112*, 5733– 5779.
17. Ashbrook, S. E.; McKay, D. Combining Solid-State NMR Spectroscopy with First-Principles Calculations - a Guide to NMR Crystallography. *Chem. Commun.* **2016**, *52*, 7186-7204.
18. Reader, S. W.; Mitchell, M. R.; Johnston, K. E.; Pickard, C. J.; Whittle, K. R.; Ashbrook, S. E. Cation Disorder in Pyrochlore Ceramics: ^{89}Y MAS NMR and First-Principles Calculations. *J. Phys. Chem. C* 2009, *113*, 18874-18883.
19. Mitchell, M. R.; Reader, S. W.; Johnston, K. E.; Pickard, C. J.; Whittle, K. R.; Ashbrook, S. E. ^{119}Sn MAS NMR and First-Principles Calculations for the Investigation of Disorder in Stannate Pyrochlores. *Phys. Chem. Chem. Phys.* **2011**, *13*, 488-497.
20. Mitchell, M. R.; Carnevale, D.; Orr, R.; Whittle, K. R.; Ashbrook, S. E. Exploiting the Chemical Shielding Anisotropy to Probe Structure and Disorder in Ceramics: ^{89}Y MAS NMR and First-Principles Calculations. *J. Phys. Chem. C* **2012**, *116*, 4273-4286.
21. Ashbrook, S. E.; Mitchell, M. R.; Sneddon, S.; Moran, R. F.; de los Reyes, M.; Lumpkin, G.; Whittle, K. R. New Insights into Phase Distribution, Phase Composition and Disorder in $\text{Y}_2(\text{Zr},\text{Sn})_2\text{O}_7$ Ceramics from NMR Spectroscopy. *Phys. Chem. Chem. Phys.* **2015**, *17*, 9049-9059.
22. Carr, H. Y.; Purcell, E. M. Effects of Diffusion on Free Precession in Nuclear Magnetic Resonance Experiments. *Phys. Rev.* **1954**, *94*, 630-638.

23. Meiboom S.; Gill, D. Modified Spin-Echo Method for Measuring Nuclear Relaxation Times. *Rev. Sci. Instrum.* **1958**, *29*, 688-691.
24. Clayden, N. J.; Dobson C. M.; Fern, A. High-Resolution Solid-State Tin-119 Nuclear Magnetic Resonance Spectroscopy of Ternary Tin Oxides. *J. Chem. Soc., Dalton Trans.* **1989**, 843-847.
25. Massiot, D.; Fayon, F.; Capron, M.; King, I.; Le Calve, S.; Alonso, B.; Durand, J. O.; Bujoli, B.; Gan Z.; Hoatson, G. Modelling One- and Two-Dimensional Solid-State NMR Spectra. *Magn. Reson. Chem.* **2002**, *40*, 70-76.
26. Orr, R. M.; Duer, M. J.; Ashbrook, S. E. Correlating Fast and Slow Chemical Shift Spinning Sideband Patterns in Solid-State NMR. *J. Magn. Reson.* **2005**, *174*, 301-309.
27. Orr, R. M.; Duer, M.; J. Applications of the CSA-Amplified PASS Experiment. *Solid State Nucl. Magn. Reson.* **2006**, *30*, 1-8.
28. Bak, M.; Rasmussen, J.; Nielsen, N. SIMPSON: a General Simulation Program for Solid-State NMR Spectroscopy. *J. Magn. Reson.* **2000**, *147*, 296-330.
29. Clark, S. J.; Segall, M. D.; Pickard, C. J.; Hasnip, P. J.; Probert, M. J.; Refson, K.; Payne, M. C. First Principles Methods Using CASTEP. *Z. Kristallogr.* **2005**, *220*, 567-570.
30. Pickard, C. J.; Mauri, F. All-Electron Magnetic Response with Pseudopotentials: NMR Chemical Shifts. *Phys. Rev. B* **2001**, *63*, 245101.
31. Perdew, J. P.; Burke, K.; Ernzerhof, M. Generalized Gradient Approximation Made Simple. *Phys. Rev. Lett.* **1996**, *77*, 3865-3868.
32. Yates, J. R.; Pickard, C. J.; Mauri, F. Calculation of NMR Chemical Shifts for Extended Systems Using Ultrasoft Pseudopotentials. *Phys. Rev. B* **2007**, *76*, 024401.
33. Green T. F. G.; Yates, J. R. Relativistic Nuclear Magnetic Resonance J-coupling with Ultrasoft Pseudopotentials and the Zeroth-Order Regular Approximation. *J. Chem. Phys.* **2014**, *140*, 234106.
34. Sturniolo, S.; Green, T. F. G.; Hanson, R. M.; Zilka, M.; Refson, K.; Hodgkinson, P.; Brown, S. P.; Yates, J. R. Visualization and Processing of Computed Solid-State NMR Parameters: MagresView and MagresPython. *Solid State Nucl. Magn. Reson.* **2016**, doi:10.1016/j.ssnmr.2016.05.004.

35. Grey, C. P.; Dobson, C. M.; Cheetham, A. K.; Jakeman, R. J. B. Studies of Rare-Earth Stannates by ^{119}Sn MAS NMR. The Use of Paramagnetic Shift Probes in the Solid State. *J. Am. Chem. Soc.* **1989**, *111*, 505-511.
36. Harvey, E. J.; Ashbrook, S. E.; Lumpkin, G. R.; Redfern, S. A. T. Characterisation of the $(\text{Y}_{1-x}\text{La}_x)_2\text{Ti}_2\text{O}_7$ System by Powder Diffraction and Nuclear Magnetic Resonance Methods. *J. Mater. Chem.* **2006**, *16*, 4665-4674.

Table 1. Calculated (using DFT) ^{119}Sn δ_{iso} for single Sn/Ti substitutions in **B**, **B^{SC}** and **C**, and relative enthalpies, ΔH .

	Model	Sn1	Sn2	Sn3	Sn4
δ_{iso} (ppm)	B	-594	-585	-610	-619
	B^{SC}	-593	-586	-606	-617
	C	-588	-583	-609	-617
ΔH / eV	B^a	0.01	0.00	0.05	0.11
	B^{SCb}	0.02	0.00	0.07	0.13
	C^b	0.05	0.04	0.07	0.14

^a ΔH relative to Sn/Ti2 substitution in **B**

^b ΔH relative to Sn/Ti2 substitution in **B^{SC}**

Figures

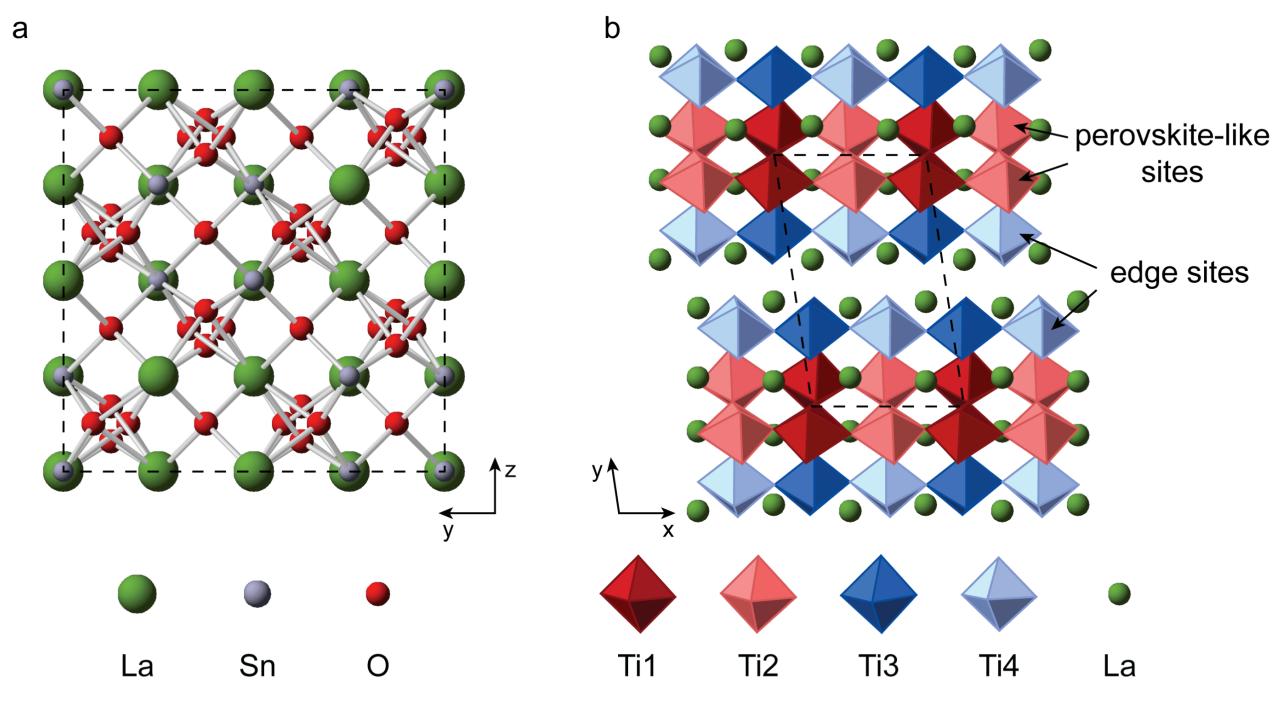


Figure 1. Structure of (a) $\text{La}_2\text{Sn}_2\text{O}_7$ pyrochlore, **A**, and (b) the monoclinic form of $\text{La}_2\text{Ti}_2\text{O}_7$ layered perovskite,⁸ **B** (with the four different Ti sites highlighted). Dashed lines indicate the unit cell. Information on the orthorhombic model of $\text{La}_2\text{Ti}_2\text{O}_7$ (**C**) is given in the Supporting Information.

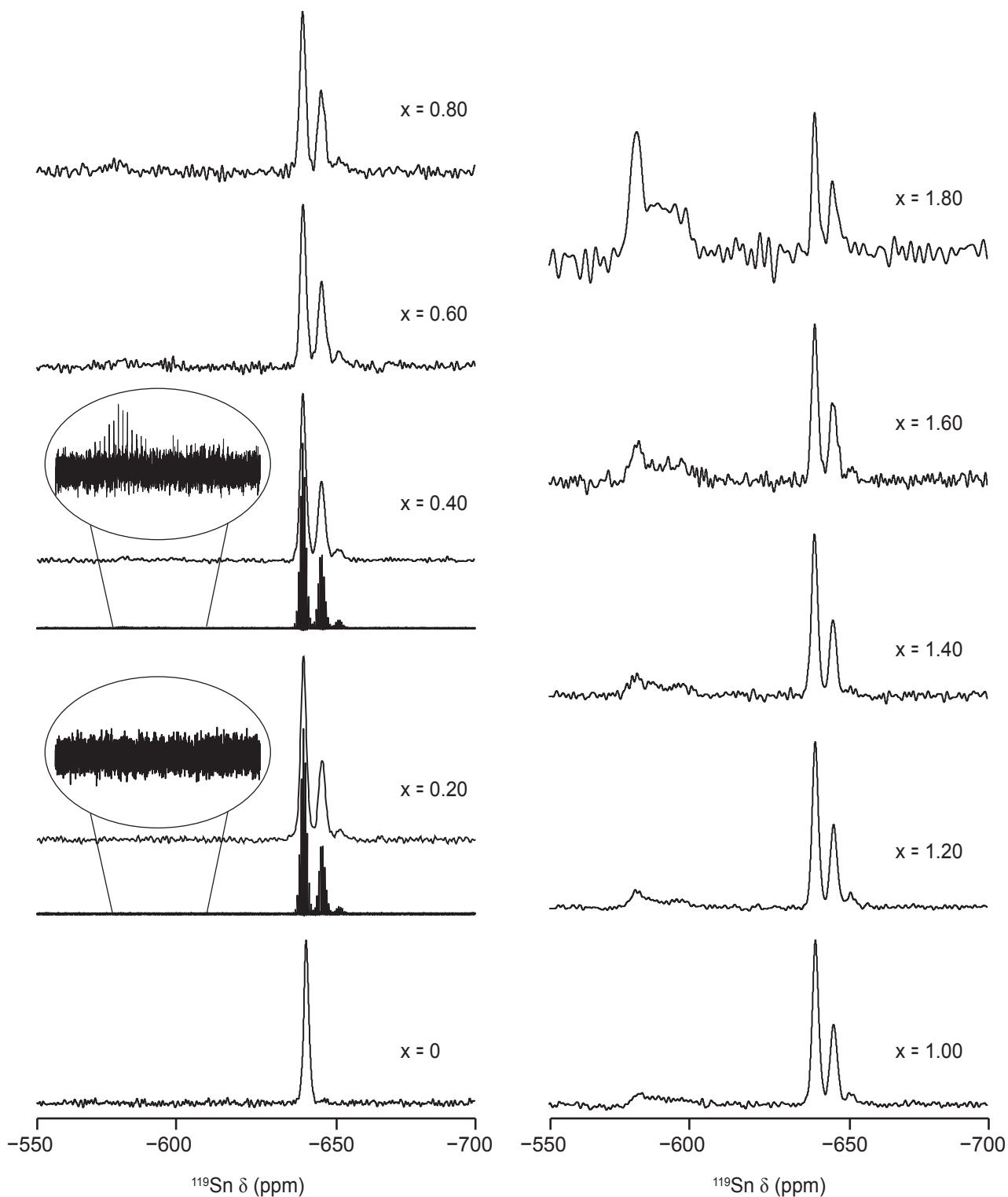


Figure 2. ^{119}Sn (9.4 T, 14 kHz MAS) NMR spectra of $\text{La}_2\text{Sn}_{2-x}\text{Ti}_x\text{O}_7$, acquired using a spin-echo pulse sequence. Additional spectra acquired with CPMG experiments are shown (as spikelets) for $x = 0.20$ and 0.40 .

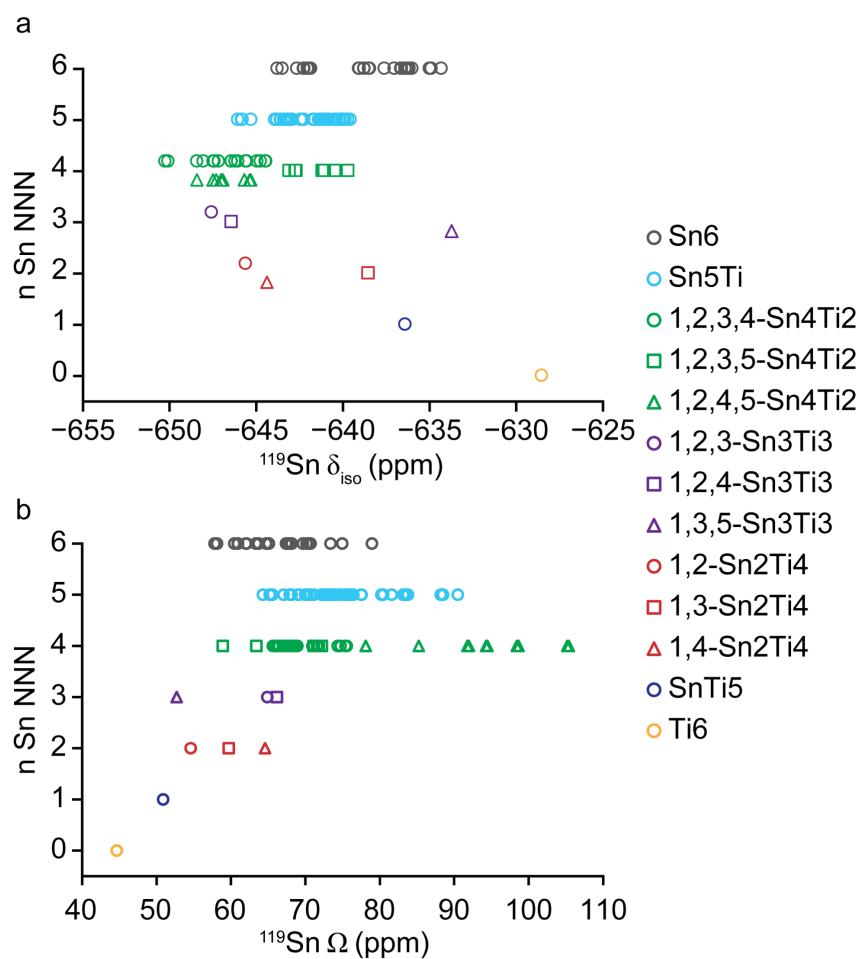


Figure 3. Plot of the number of Sn NNN against (a) calculated $^{119}\text{Sn} \delta_{\text{iso}}$ and (b) calculated $^{119}\text{Sn} \Omega$ for Ti substitution into the pyrochlore B sites. See the Supporting Information for details of the nomenclature.

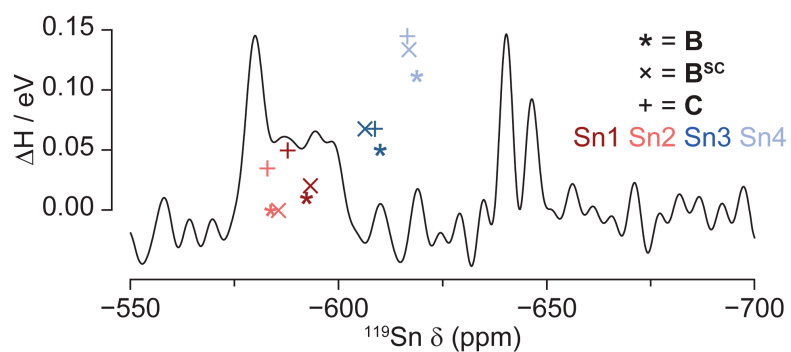


Figure 4. Plot of relative enthalpy (ΔH) against calculated ^{119}Sn δ_{iso} for Sn substitutions in **B** (*), **B^{SC}** (x) and **C** (+) with overlay of the experimental ^{119}Sn MAS NMR spectrum for the sample with nominal composition $\text{La}_2\text{Sn}_{0.2}\text{Ti}_{1.8}\text{O}_7$. ΔH values are relative to Sn2/Ti2 substitution for **B** and Sn2/Ti2 substitution in **B^{SC}** for both **B^{SC}** and **C** series.

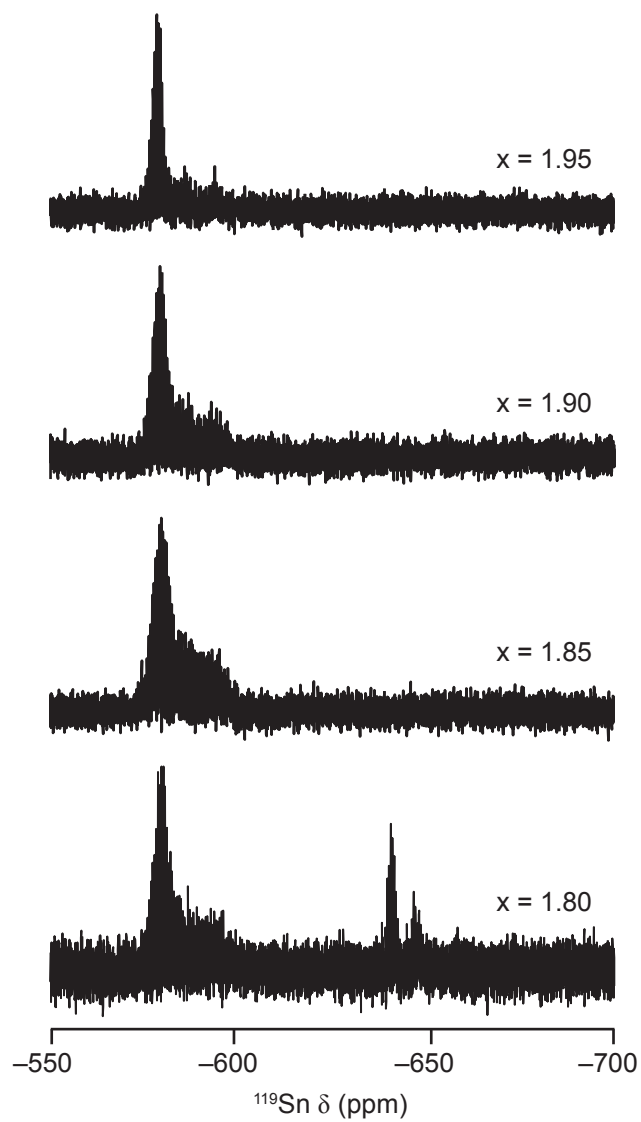


Figure 5. ^{119}Sn (9.4 T, 14 kHz MAS) CPMG NMR spectra (shown as spikelets) of $\text{La}_2\text{Sn}_{2-x}\text{Ti}_x\text{O}_7$ with x from 1.80 to 1.95.

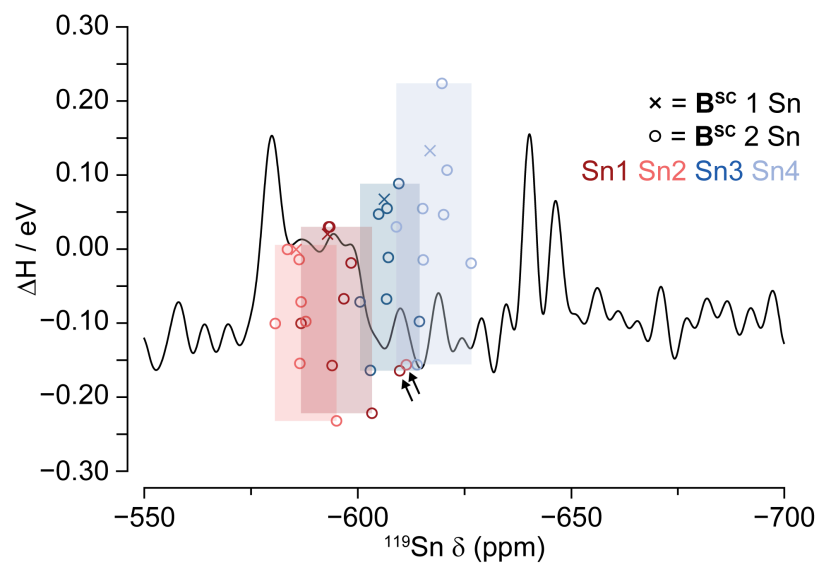


Figure 6. Plot of relative enthalpy (ΔH) against calculated $^{119}\text{Sn } \delta_{\text{iso}}$ for mono- and di-substituted \mathbf{B}^{SC} models showing the spread associated with di-substituted structures. Sn1 and Sn2 models that fall outside their typical shift ranges are indicated (see the main text for details).

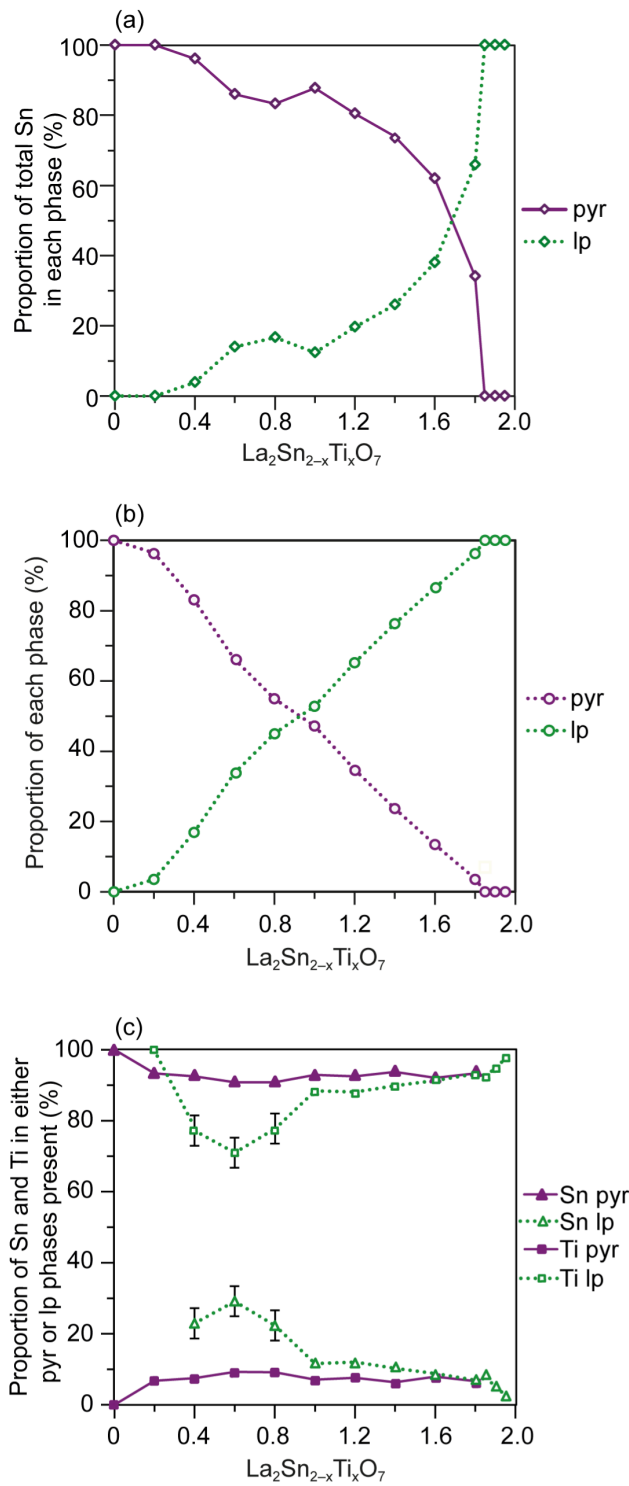


Figure 7. Plots showing (a) the proportion of Sn found in the pyrochlore (pyr) and layered perovskite (lp) phases, (b) the total proportion of pyr and lp phases present in the sample and (c) the composition of the two phases, as a function of the nominal composition used in the initial synthesis. In (c), the percentages of the Sn and of the Ti in the pyrochlore phase (or the layered perovskite phase) should equal 100%.

TOC graphic

